PHYSICAL REVIEW B VOLUME 34, NUMBER 6 15 SEPTEMBER 1986

Profile structures of very thin multilayers by x-ray diffraction using direct and refinement methods of analysis

Victor Skita*
Department of Biochemistry and Biophysics, University of Pennsylvania, Philadelphia, Pennsylvania 19104-6323

Mark Filipkowski
Department of Physics, University of Pennsylvania, Philadelphia, Pennsylvania 19104-6396

Anthony F. Garito
Department of Physics, University of Pennsylvania, Philadelphia, Pennsylvania 10104-6396
and Laboratory for the Research on the Structure of Matter, University of Pennsylvania,
Philadelphia, Pennsylvania 19104-3859

J. Kent Blasie
Department of Chemistry and Department of Biochemistry and Biophysics, University of Pennsylvania,
Philadelphia, Pennsylvania 19104-6323
and Laboratory for the Research on the Structure of Matter, University of Pennsylvania, Philadelphia, Pennsylvania 19104-3859

(Received 11 November 1985)

Meridional x-ray diffraction data from Langmuir-Blodgett multilayers containing two to ten molecular monolayers of arachidic acid were analyzed by two independent methods. A Patterson-function deconvolution technique uniquely provided the electron density profile (8 Å resolution) of the average, symmetric bilayer repeated in the multilayer. This average bilayer appeared to disorder as the number of bilayers in the multilayer decreased. A refinement technique uniquely provided the profile structure of the multilayer itself; in particular, it could distinguish the individual monolayers in the multilayer. The refinement demonstrated that only one of the monolayers (either the first or the last monolayer in the deposition sequence) in each multilayer was disordered.

I. INTRODUCTION

X-ray diffraction can in principle be used to investigate the structure of very thin multilayer films containing only a few molecular monolayers deposited on solid substrates by the Langmuir-Blodgett technique. One would like to ascertain whether the structures of the individual monolayers differ from one another and particularly whether the substrate perturbs certain individual monolayers in the multilayer film. Previous analyses of the meridional x-ray diffraction from such multilayer films have employed either a nonunique modeling of the multilayer electron density profile to fit the observed diffraction data[1] or direct methods (multilayer profile Patterson-function deconvolution[2] and counter-ion isomorphous replacement[3] to uniquely derive the electron density profile of the average, symmetric bilayers, or bilayer pairs repeated N times in the multilayer.

We have collected accurate meridional x-ray diffraction data from multilayers containing one, two, three, and five bilayers of a fatty acid deposited on alkylated glass substrates. Data from these multilayers were analyzed by two independent methods for comparative purposes. A Patterson-function deconvolution technique[2] provided uniquely the electron density profiles (8 Å resolution) of the average, symmetric bilayer as a function of the number of times N ($N=2,3,5$) it was repeated in the multilayer. A box-refinement technique[4,5] for the homologous series of multilayer structures $N=1,2,3$ uniquely provided the electron density profile (8 Å resolution) of the multilayer itself, namely, of each individual monolayer as a function of its position in the three multilayers.

II. METHODS

Multilayer samples were prepared by depositing successive monolayers of arachidic acid using the Langmuir-Blodgett technique[6] onto a flat glass substrate coated with a covalently bound octadecyltrichlorosilane (OTS) (Ref. 7) monolayer. The arachidic acid (Aldrich) had been zone refined with 50 zone passes at a rate of 1 cm/hr and the purity ($>99.995\%$) of the center fraction confirmed by differential scanning calorimetry (DSC) measurements (Dupont 990). Triple distilled water (Millipore) was used in all stages of the preparation, including distillation over $KMnO_4$ to remove organic contaminants. A Lauda Langmuir trough system was used for the deposition. The arachidic acid monolayer was kept at a constant surface pressure of 20 dyn/cm and a temperature of 17.5 °C during the deposition; the subphase was a 1 mM $CdCl_2$ solution with an air equilibrated $p\mathrm{H}<6.0$. The substrate was dipped through the monolayer at a rate of 0.3 cm/min.

Since the OTS glass substrate is hydrophobic (due to the covalently attached alkane chains), a monolayer of arachidic acid is deposited onto the substrate surface as the substrate is lowered through the arachidic acid monolayer into the subphase. As the specimen (its surface now hydrophilic from the fatty-acid carboxyl groups) is raised from the subphase through the arachidic acid monolayer, a second monolayer of fatty acid is deposited onto the substrate, leaving a hydrophobic surface. This process may be repeated several times to create a variable number N of arachidic acid bilayers. The multilayer specimens in this study consisted of one, two, three, and five arachidic acid bilayers.

Meriodional $(00l)$ x-ray diffraction was observed as a function of q_z [$|q_z| \equiv (2\sin\theta)/\lambda$] corresponding to elastic momentum transfers parallel to the z axis perpendicular to the substrate plane. This meridional x-ray diffraction arises from the projection of the three-dimensional

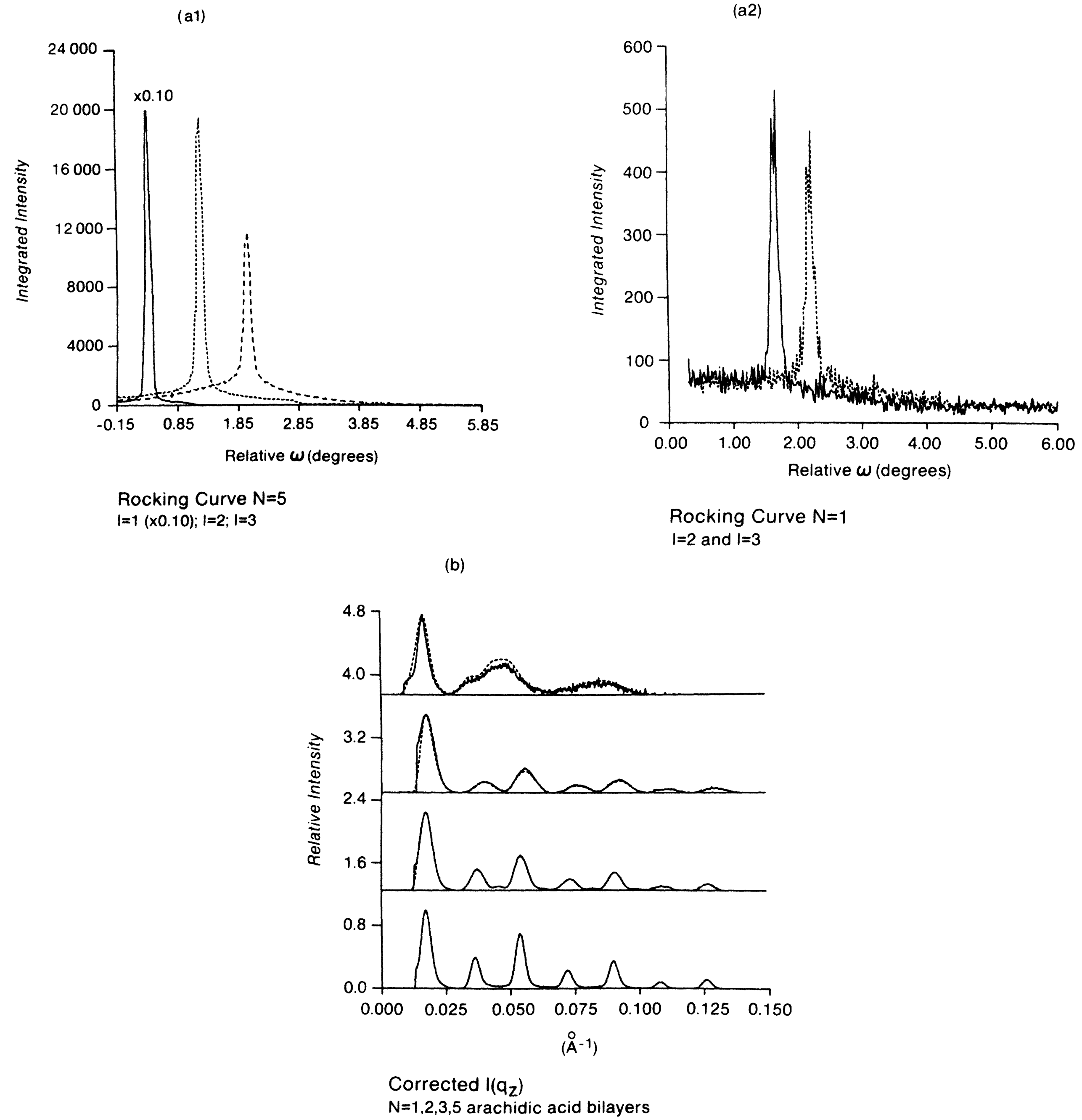

FIG. 1. (a) Rocking curves for the five-bilayer multilayer are shown in (A1) with the solid line the rocking curve for $h=1$ *(attenuated by a factor of 10)*, the dotted line the rocking curve for $h=2$, and the dashed line the rocking curve for $h=3$. The rocking curves for the one-bilayer multilayer are shown in (A2) with the dotted line the rocking curve for $h=2$ and the dashed line the rocking curve for $h=3$. (b) Lorentz q_z-corrected, meridional intensity functions for one-, two-, three-, and five-bilayer arachidic acid multilayers *(from top to bottom)* are shown by the solid line. The first maxima of the corrected intensity functions have been scaled to unity. The dotted lines (for $N=1,2,3$) represent intensity functions calculated from the multilayer electron density profiles derived by the box-refinement techniques.

multilayer electron density distribution along radial vectors lying in the layer planes perpendicular to the z axis onto the z axis; the projection is defined as the electron density profile for the multilayer. The incident x-ray beam defines an angle omega (ω) with the substrate plane (x-y). For coherent elastic scattering, the modulus of the incident momentum vector ($\mathbf{k}_i$) equals the modulus of the scattered momentum vector ($\mathbf{k}_s$); this requires ω to equal θ, where 2θ is the angle between the incident and scattered beams.

The multilayers were positioned on the ω axis of a Hüber two-axis diffractometer with a low-impedance, position-sensitive linear detector (PSD) mounted on the 2θ axis. The linear detector was aligned along the q_z direction. A rotating-anode x-ray generator (Elliott GX-6) was used to produce Cu K x rays at a target loading of ~ 2.5 kW/mm^2. Nickel filters were used to select the Cu $K\alpha$ line which was line focused parallel to the multilayer plane with Franks optics. X-ray beam width and the PSD system resolution result in a Δq_z resolution of ~ 0.003 Å^{-1}. The full beam line height (3 mm) was accepted by the PSD over the entire q_z range for the multilayer specimens investigated due to their small mosaic spread (see below).

Specimens were kept at room temperature (23—25 °C) and at a relative humidity of $<0.1\%$ in a sealed canister. Helium paths with thin aluminum foil windows were used to reduce air scattering along the incident and scattered beam paths.

ω scans ($\Delta\omega = 0.02°$) consisting of two minute exposures per omega value were performed on each specimen over an omega range from $\sim 0.5°$ to $6.5°$. Each full scan took approximately 10 h and was controlled by a Digital Equipment Corporation PDP11/24 minicomputer. The sum of these exposures form a composite pattern which represents the meridional intensity function $I(q_z)$. As the value of omega is decreased below $\sim 0.8°$, specular scattering due to the glass OTS surface predominates and begins to saturate the detector. Scattering in this region of momentum-transfer space arises only from the substrate and the interference between arachidic acid bilayers and the substrate.

A plot of the integrated intensity of a diffraction maximum at $q_z \sim h/d$, where h is an integer and d is the average periodicity in angstroms of the multilayer projected onto the z axis, versus ω gives a "rocking curve" for diffraction maximum h whose full width at half maximum (FWHM) is a measure of the mosaic spread of the multilayer. Rocking curves for $h = 1,2,3$ for $N = 5$ and $h = 2,3$ for $N = 1$ are shown in Fig. 1(a). The rocking curve for the first maximum for $N = 1$ could not be measured as accurately since the specular scattering contributes considerable intensity in the region of momentum-transfer space $q_z \sim 1/d$ for this multilayer. Each rocking curve is a composite of a strong, narrow feature at $\omega = \theta_h$ for diffraction maxima h centered on a weak, broad feature extending over $0° \leq \omega \leq 2\theta_h$. The measured mosaic spread for the narrow feature in each rocking curve is $\sim 0.13°$ and is $\sim 1.50°$ for the broad feature. The measured mosaic spread of the specular scattering from a OTS glass substrate alone is $\sim 0.08°$ *(data not shown).* Since the beam is focused along q_z at the face of the detector, beam convergence at the specimen contributes to the measured mosaic spread of the multilayers.

As mentioned above, specular scattering due to the OTS glass substrate predominates the meridional intensity function at $q_z \leq \sim 0.02$ Å^{-1}. We have investigated the intensity function derived from an OTS glass sample alone, and have found it possible to fit this function with two exponentials over the range of q_z utilized in these studies. A quickly decaying exponential can be fit to the very low-angle OTS glass specular scattering, while a slowly decaying exponential function can be fit to the higher-angle part of the intensity function to correct for substrate background scattering. Similar exponentials were used to correct the meridional intensity functions of the one-, two-, three-, and five-bilayer multilayer specimens. The first observable diffraction maxima of the intensity function for the one-bilayer specimen appears as a shoulder at $q_z \sim 0.02$ Å^{-1} on the more intense specular scattering at smaller q_z. This shoulder can be resolved by subtracting the quickly decaying exponential of the specular scattering from the intensity of the one-bilayer sample. The intensity functions for the two-, three-, and five-bilayer samples exhibit a much better resolved first-order diffraction maximum. This occurs since the contribution to the intensity function from the multilayer increases quadratically with the number of bilayers, while the contribution from the specular scattering stays nearly the same. This background scattering correction causes unavoidable errors in determining the relative magnitude and shape of the first diffraction maximum especially for the one-bilayer specimen. Data from one-bilayer samples collected with a silicon-intensified target (SIT) two-dimensional detector[8,9] using synchrotron radiation aided in the background scattering correction for the one-bilayer data due to the very different two-dimensional shapes of the diffraction maxima observed for the specimen and the specular scattering from the substrate.

A Lorentz correction of q_z was applied to the intensity function to correct for the oscillation of the multilayer in the ω scan. Since the specimens have a thickness ranging between ~ 50 and 300 Å, no absorption correction is required for the ω range used. The q_z Lorentz correction fixes the origin in momentum-transfer space, errors in which will change the relative magnitudes of the diffraction maxima in the corrected intensity function, $I_0(q_z)$. For the two-, three-, and five-bilayer data sets, a plot of the diffraction order number versus the center of mass of the meridional diffraction maximum in channels gives a reasonable first estimate of the origin as the x intercept. A good approximation of the average periodicity of the multilayer profile can be deduced from the slope.

III. RESULTS

The corrected meridional intensity function for a multilayer composed of repeated unit cells containing a bilayer with a unit-cell translation vector along the z direction of magnitude d is given by the following equation (see, for example, Hoseman and Bagchi[10]):

$$I_0(q_z)\propto |F_{UC}(q_z)|^2|L_n(q_z)|^2 * W(q_z)\ , \qquad (1)$$

with $*$ denoting the convolution product, where

$$|L_n(q_z)|^2=\sum_{h=-\infty}^{\infty}\delta(q_z-h/d)*|B(q_z)|^2 \qquad (2)$$

and $F_{UC}(q_z)$ is the unit-cell profile structure factor; $|L_n(q_z)|^2$, the reciprocal lattice or interference function for the multilayer profile; $B(q_z)$, the Fourier transform of the multilayer profile box function; and $W(q_z)$, the incident beam-shape function. The multilayer profile structure factor, $F_{ml}(q_z)$, is given by

$$F_{ml}(q_z)=F_{UC}(q_z)L_n(q_z)\ . \qquad (3)$$

Figure 1(b) shows the corrected meridional intensity functions for one-, two-, three-, and five-bilayer arachidic acid specimens. Note that as the number (N) of bilayers decreases the diffraction maxima broaden, until continuous diffraction is observed for $N=1$. Also observe the shifting of the diffraction maxima. As N decreases, diffraction orders two and three, four and five, shift together.

As the number of bilayers increases to large N, the Fourier transform of the multilayer profile box function $B(q_z)$ approaches a Dirac δ function. The reciprocal lattice or interference function $|L_n(q_z)|^2$ in turn becomes an infinite series of δ functions spaced at $1/d$ along the q_z axis. The intensity function $I_0(q_z)$ is then simply the modulus squared of the unit-cell structure factor sampled at $1/d$ along q_z and convoluted with the beam-shape function. This limit is Bragg diffraction. For finite multilayer specimens $B(q_z)$ is a sinc function [where $\text{sinc}(x)\equiv\sin(x)/x$] of pseudoperiod $2/Nd$. The intensity function will thus contain diffraction ordres whose centers of mass occur near the Bragg limit, but may be shifted since the unit-cell structure factor modulus is not being sampled by δ functions. [Taking the derivative of Eq. (1), assuming $W(q_z)=\delta(q_z)$ yields

$$\frac{dI_0}{dq_z}\propto 2F_{UC}L_n\left[F_{UC}\frac{dL_n}{dq_z}+L_n\frac{dF_{UC}}{dq_c}\right]\ .$$

For $I_0(q_z)$ to be a maximum requires

$$F_{UC}\frac{dL_n}{dq_z}+L_n\frac{dF_{UC}}{dq_z}=0\ .$$

From Eq. (2), we see that L_n is a maximum at $q_z=h/d$. For diffraction maxima to be located at the Bragg locations (i.e., when L_n is a maximum and $dL_n/dq_z=0$) $dF_{UC}/dq_z=0$ from the above equation; otherwise the diffraction maxima will be shifted.] The diffraction orders are broad because the unit-cell structure factor modulus is being sampled by a set of sinc^2 functions arising from the Fourier transform of the autocorrelation of the multilayer profile box function (see below). As the number of bilayers decreases, there is a corresponding broadening and shifting of the diffraction maxima until $N=1$, at which point the meridional diffraction $I_0(q_z)$ is no longer sampled [$|L_n(q_z)|^2\to\text{const}$] and the diffraction that is observed represents the modulus squared of the unit-cell or bilayer structure factor convoluted with the beam-shape function.

The Fourier transforms of Eqs. (1) and (2) yield both the multilayer profile Patterson function $P_{ml}(z)$ (i.e., the multilayer profile autocorrelation function),

$$P_{ml}(z)=\{[\rho_{UC}(z)*l_n(z)]*[\rho_{UC}(-z)*l_n(-z)]\}w(z) \qquad (4)$$

and the multilayer profile lattice autocorrelation function, respectively, $\tilde{l}_n^2(z)$,

$$\tilde{l}_n^2(z)=\sum_{n=-\infty}^{+\infty}\delta(z-nd)\tilde{b}^2(z)\ , \qquad (5)$$

where $\rho_{UC}(z)$ is the average unit-cell electron density profile; $b(z)$, the multilayer profile box function; $w(z)$, the Fourier transform of the beam-shape function; and $\tilde{l}_n^2(z)$ and $\tilde{b}^2(z)$ represent the autocorrelation of $l_n(z)$ and $b(z)$, respectively.

In addition, the Fourier transform of the multilayer structure factor $F_{ml}(q_z)$ yields the multilayer electron density profile, $\rho_{ml}(z)$ [refer to Appendix A of Ref. 11 for a complete derivation of Eq. (6)]:

$$\rho_{ml}(z)=\rho_{UC}(z)*\langle l_n(z)\rangle\ . \qquad (6)$$

The multilayer box function $b(z)$ is unity for $-D/2<z\leq D/2$ and is zero otherwise where $D=Nd$. D therefore is the total extent of the multilayer projected along z in real space.

The Patterson functions $P_{ml}(z)$ for the one-, two-, three-, and five-bilayer specimens are shown in Fig. 2. Note that the Patterson function is sensitive to the total extent of the multilayer along the z axis. To a first ap-

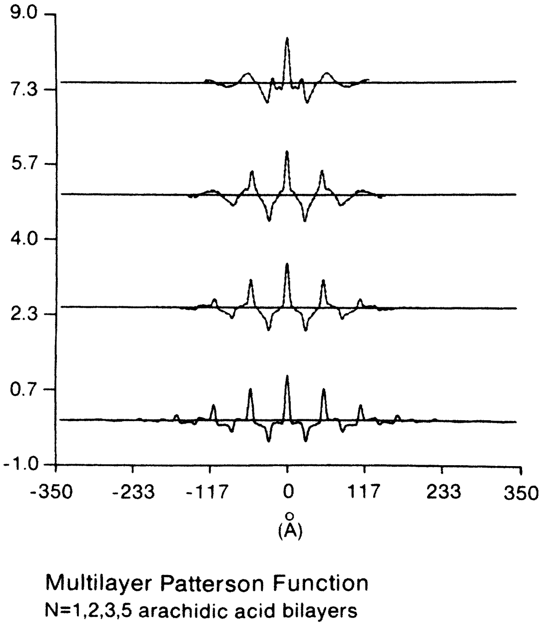

FIG. 2. Multilayer profile Patterson functions for one-, two-, three-, and five-bilayer arachidic acid multilayers *(from top to bottom)* are shown by the solid lines. The dotted lines (for $N=1,2,3$) represent the multilayer profile Patterson functions calculated from the multilayer electron density profiles obtained by the box-refinement procedure.

proximation, the Patterson functions are pseudoperiodic and decay nearly linearly to zero at $z=\pm Nd$ due to $\tilde{b}^2(z)$ [Eqs. (4) and (5)]. This property of $P_{\mathrm{ml}}(z)$ was used iteratively to refine the origin of $I_0(q_z)$. Some "ringing" in the Patterson function for $z \geq \pm Nd$ is a result of uncertainties in determining the magnitude and shape of the first maximum in the corrected intensity functions and the truncation of the data for $q_z < 0.01$ Å^{-1}. Reasons for these uncertainties were discussed above.

The shifting and broadening of the diffraction maxima [Fig. 1(b)] are a direct consequence of $b(z)$. The intensity and Patterson functions are thus sensitive to the number N of bilayers in a given multilayer thin film for sufficiently small N relative to $W(q_z)$.

Due to the intense specular scattering from the substrate, the intensity functions were truncated at $q_z \sim 0.01$ Å^{-1}. Thus, the electron density profiles derived below represent relative and not absolute electron densities.

IV. ANALYSIS

Equation (4) can be rewritten to yield

$$P_{\mathrm{ml}}(z)=\{[\rho_{\mathrm{UC}}(z)*\rho_{\mathrm{UC}}(-z)]*[l_n(z)*l_n(-z)]\}w(z)\,,$$
$$=[P_{\mathrm{UC}}(z)*\tilde{l}_n^2(z)]w(z)\,, \qquad (7)$$

where $P_{\mathrm{UC}}(z)$ is the unit-cell Patterson function or equivalently the autocorrelation of the unit-cell electron density profile. It is possible to uniquely reconstruct the unit-cell Patterson $P_{\mathrm{UC}}(z)$ provided that $\tilde{l}_n{}^2(z)$, and consequently $P_{\mathrm{ml}}(z)$ is bounded.[11,12] If one assumes $\rho_{\mathrm{UC}}(z)$ to be centrosymmetric around an origin [i.e., $\rho_{\mathrm{UC}}(z)=\rho_{\mathrm{UC}}(-z)$] $P_{\mathrm{UC}}(z)$ in turn can be deconvoluted uniquely to give the electron density profile $[\rho_{\mathrm{UC}}(z)]$ for the unit cell (or the average bilayer in the multilayer) by a recursive deconvolution method.[2,11] However, this recursive deconvolution propagates errors. The final electron density profile is obtained by phasing (see below) the Lorentz-corrected intensity function $[I_0(q_z)]$ and selecting the best phase combination which is most consistent with the electron density profile for the unit cell derived by the recursive deconvolution method.

In general, for both the multilayer and unit-cell electron density profiles assuming $W(q_z)=\delta(0)$,

$$\rho_{\mathrm{ml}}(z) \propto \int_{-\infty}^{+\infty} F_{\mathrm{ml}}(q_z)\exp(2\pi i q_z z)dq_z\,, \qquad (8)$$

where

$$F_{\mathrm{ml}}(q_z)=|F_{\mathrm{ml}}(q_z)|\exp[i\phi(q_z)]$$

and

$$I_0(q_z) \propto |F_{\mathrm{ml}}(q_z)|^2\,.$$

Since we assume that the bilayer profile is centrosymmetric, the phase $\phi(q_z)$, can have values of only 0 or π. Thus, Eq. (8) becomes

$$\rho_{\mathrm{ml}}(z) \propto 2\int[\pm|F_{\mathrm{ml}}(q_z)|\cos(2\pi z q_z)]dq_z\,. \qquad (9)$$

$\phi(q_z)$ can only change phase if $F_{\mathrm{ml}}(q_z)$ equals zero for that value of q_z; otherwise $F_{\mathrm{ml}}(q_z)$ would be multivalued. Thus the number of possible phase combinations is 2^h

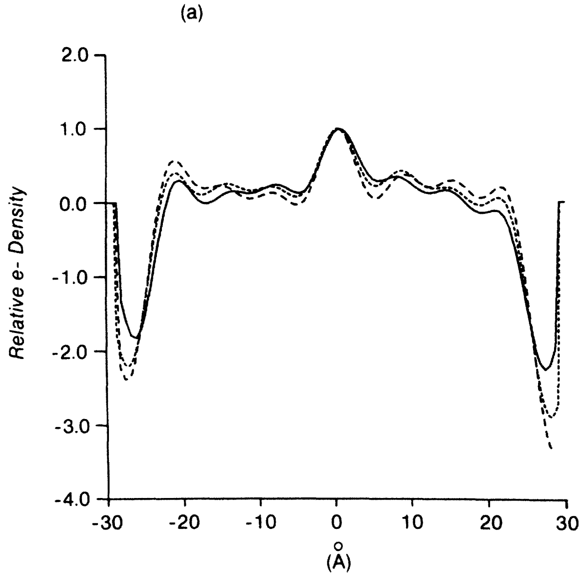

Unit Cell Deconvolution
N=2,3,5 arachidic acid bilayers

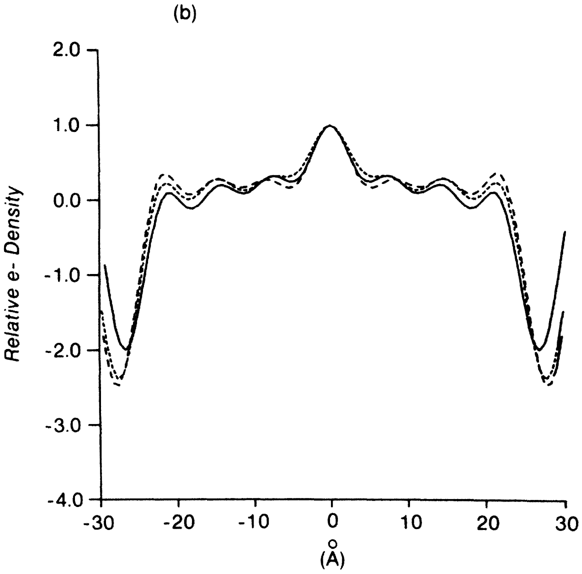

Fourier Synthesis
N=2,3,5 arachidic acid bilayers

FIG. 3. (a) Electron density profiles for the average bilayer for the five- (— — — —), the three- (— — —), and the two- (———) bilayer arachidic acid multilayers derived by unit-cell Patterson recursive deconvolution method. The profiles have been normalized so that the relative electron densities of the polar head groups are the same. The recursive errors propagate from right to left in the figure. (b) Electron density profiles for the average bilayer for the five- (— — — —), the three- (— — —), and the two- (———) bilayer arachidic acid multilayers derived by a correctly phased Fourier synthesis. The profiles have been normalized so that the relative electron densities of the polar headgroups are the same.

where h is the number of observed diffraction maxima. (Since half of the solutions differ by a shift in the z origin by $d/2$, the effective number of solutions is 2^{h-1}.)

Figure 3(a) shows the electron density profiles for the average bilayer for the two-, three-, and five-bilayer multilayers derived by the unit-cell Patterson recursive deconvolution outlined above. Errors in these profiles propagate from right to left; hence the asymmetry of the functions.

Figure 3(b) shows the electron density profiles for the average bilayer for the two-, three-, and five-bilayer multilayers derived by the correctly phased Fourier synthesis via Eq. (9). All three rather typical electron density profiles exhibit (i) a peak region of relatively high electron density for $0.0 \le |z| \le 4.5$ Å containing the —COOH polar headgroups; (ii) plateau regions of intermediate relative electron density near the mean for $4.5 \le |z| \le 21.0$ Å containing the hydrocarbon chain [—$(CH_2)_{18}$—] groups; and (iii) trough regions of relatively low electron density for $21.0 \le |z| \le 29.5$ Å containing the terminal methyl groups (—CH_3). For these bilayers, the multilayer periodicity is the methyl group separation across the bilayer profile. Note the close similarity in detail of the profiles derived by recursive deconvolution and those derived by the correctly phased Fourier synthesis.

As N decreases, there is a corresponding decrease in the multilayer periodicity of the average bilayer profiles as evidenced by the decrease in the methyl group separation distance across the bilayer profile. For $N=5,3,2$, the periodicities are 55.9, 54.4, and 52.9 Å, respectively. In addition to a decrease in multilayer periodicity, a broadening of the methyl trough regions into the neighboring hydrocarbon chain plateau regions and a subsequent decrease in the depth of the methyl trough regions are observed as the number of bilayers decreases. These changes in the hydrocarbon core region of the average bilayer profile with decreasing N are similar to those accompanying "kink" formation (time average or ensemble average) in *all trans* hydrocarbon chains. For example, Fig. 4 shows the electron density profiles for a dipalmitoyl phosphatidyl choline (PC) bilayer at 35 and 49 °C, the former being below the phase transition temperature for chain melting of 41 °C, the latter above. Note that within the hydrocarbon core regions of the profiles, the melted PC profile (dashed line) exhibits many of the features (due to the time-average kink formation in the fatty-acid chains) of the $N=2$ electron density profile of arachidic acid while the frozen PC profile displays the features (due to the *all trans* configuration of the fatty-acid chains) of the $N=5$ electron density profile of arachidic acid. In particular, note the similarly decreased average hydrocarbon chain length and broadened methyl trough features in both the melted PC and arachidic acid $N=2$ electron density profiles.

The assumption that the electron density profile for a bilayer structure is centrosymmetric and repeated N times in the multilayer profile becomes less valid as the number of bilayers in the multilayer thin film decreases. The fact that the background scattering corrected intensity function $[I_0(q_z)]$ for $N=2$ and 3 [Fig. 1(b)] is substantially nonzero between some adjacent diffraction maxima strongly suggests that the corresponding multilayer electron density profile may be asymmetric. [For centrosymmetric multilayer electron density profiles, the intensity function can have nonzero minima if and only if the phase $\phi(q_z)$ does not change across the minima. Otherwise the structure factor, $F_{\mathrm{ml}}(q_z)$, is multivalued at the minima. The unit-cell electron density profiles derived by the Patterson-function deconvolution method require a phase change at these nonzero maxima.] A model for the multilayer electron density profile for $N=2$ can be constructed by extending the electron density profile for the average bilayer (Fig. 3) to two bilayers (dotted line, Fig. 5). This centrosymmetric model for the multilayer profile yields the intensity function shown by the dotted line in Fig. 6. This figure shows the derived intensity function after convolution with the incident beam-shape function, $W(q_z)$. The intensity function shows auxiliary maxima between major diffraction orders; convolution with $W(q_z)$ suppresses the secondary maxima and introduces a nonzero "baseline" to the intensity function. [The auxiliary or secondary maxima arise from the Fourier transform of the multilayer box function, which is a sinc function. See Eqs. (1) and (2).] Note that all the minima in the calculated intensity function for this centrosymmetric model are zero with respect to this baseline.

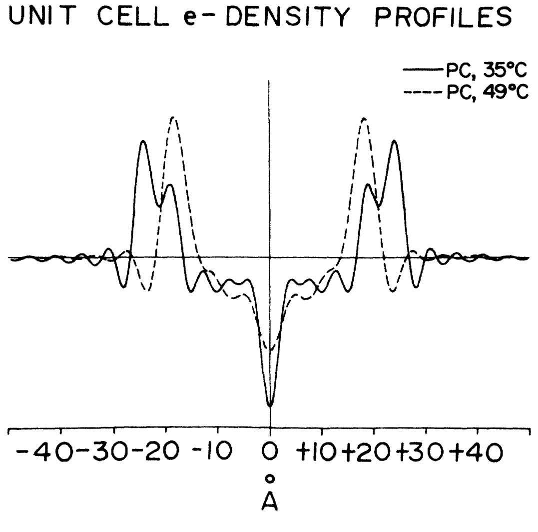

FIG. 4. Unit-cell electron density profile for a dipalmitoyl phosphatidyl choline (PC) bilayer at 35 and 49 °C. The former is below the phase transition temperature for chain melting, the latter above. [Figure 4 is reproduced by courtesy of J. K. Blasie from J. Cain, G. Santillan, and J. K. Blasie, Proceedings of 1972 ICN-UCLA Symposium on Molecular Biology, in *Membrane Research*, edited by C. F. Fox (Academic, New York).]

This direct Patterson-function deconvolution method outlined above is limited in that it determines only the electron density profile of the average unit cell or bilayer in the multilayer. It cannot accommodate bilayer structures where the monolayer profile structures differ from one another; in particular, it cannot distinguish between the first monolayer on the alkylated substrate as compared to the last monolayer at the air interface. In gen-

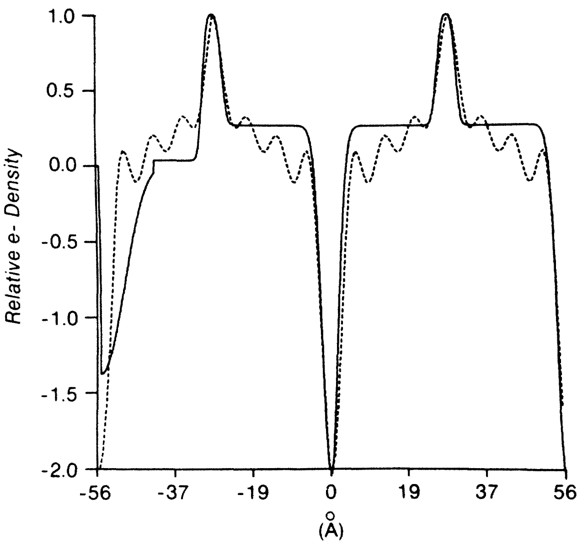

Model Electron Densities
Symmetric and asymmetric models (N=2)

FIG. 5. Two model multilayer electron density profiles for the two-bilayer multilayer are shown. The dotted line represents a symmetric model based on the repetition of the derived electron density profile for the average bilayer from the Patterson-function deconvolution procedure (Fig. 3); the solid line is an asymmetric model based on the box-refinement multilayer profile (Figs. 7 and 8).

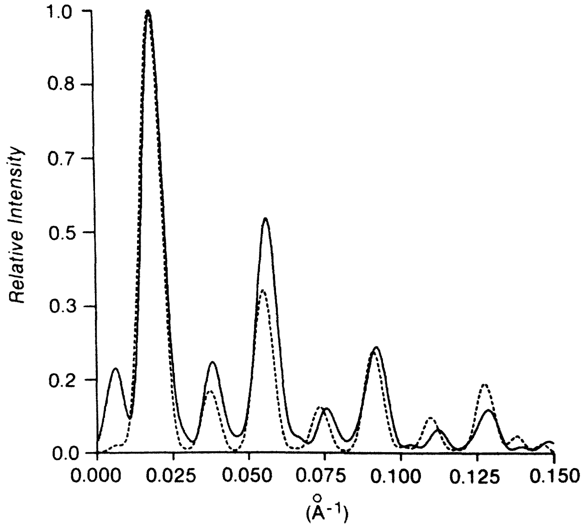

Symmetric and Asymmetric Model
Convoluted intensities (N=2)

FIG. 6. Meridional intensity functions (after convolution with the incident beam-shape function) derived from the model multilayer electron density profiles for the two-bilayer multilayer shown in Fig. 5. The dotted line represents $I(q_z)$ derived from the symmetric model. Note the zero-level minima (with respect to a nonzero baseline, see text) between diffraction maxima. The solid line represents $I(q_z)$ derived from the asymmetric model. The minima between diffraction maxima two and three, and four and five are clearly nonzero. The first diffraction maxima in each function has been normalized to one.

eral, it is impossible to phase asymmetric structures of infinite extent ($N>10$, dependent on the experimental system x-ray optics) unless some special technique (e.g., isomorphous replacement) is employed. However, for finite systems (i.e., where the one-dimensional Fourier transform of the corrected intensity function $[I_0(q_z)]$ gives a bounded Patterson function $[P_{\rm ml}(z)]$) (see Fig. 2) the box-refinement procedure can be used to determine the multilayer electron density profile $\rho_{\rm ml}(z)$[4].

This technique assumes a given phase for each point in q_z derived from the Fourier transform of some arbitrary "trial" function. These phases are combined with the modulus of the multilayer structure factor $|F_{\rm ml}(q_z)|$ and Fourier transformed to give an initial electron density profile $\rho_{\rm ml}(z)$. This electron density profile is in turn set to zero outside a box $b(z)$ whose width is at least that of the multilayer profile. This truncated electron density profile becomes the new trial function and the process is repeated iteratively until the the refinement converges. [As noted earlier, the intensity function, and thus $|F_{\rm ml}(q_z)|$ are sensitive to the finite extent of the sample. The broadening and shifting of the intensity maxima from the Bragg limit provide this information.] The width of the box $b(z)$ can be determined from the multilayer patterson function; $P_{\rm ml}(z)$ must be zero for $|z|$ larger than the maximum extent of $\rho_{\rm ml}(z)$ due to $b(z)$. It is the finite extent of the multilayers in z that provide the strong constraint needed for the box-refinement technique to coverage to a solution for the multilayer profile $\rho_{\rm ml}(z)$. The refinement continues until it has found a phase combination that will produce a multilayer electron density profile which is zero outside the box. Unfortunately there is no guarantee that the solution derived from the box refinement is unique; in fact, there are likely to be several "local" solutions that satisfy the box constraint.[5] The final solution may ultimately depend to some extent on the initial trial function The trial function used in this analysis was the sum of a cosine and sine wave with a wavelength on the order of twice the total extent of the multilayer profile as derived from the multilayer Patterson function. Various other trial functions were also analyzed such as ramp functions of various sizes and pulse functions of different widths, which refine to qualitatively similar multilayer profile structures.

The one-, two-, and three-bilayer multilayer systems were investigated with the box-refinement technique. The three corrected intensity functions $I_0(q_z)$ were refined to multilayer electron density profiles which exhibited features common to each multilayer electron density profile, as well as exhibited features common to each monolayer within the multilayer electron density profiles. Figure 7 shows the resulting multilayer electron density profiles (i.e., continuous profiles) for $N=1,2,3$ after 20 iterations from the box-refinement technique. The figure also shows the trial function used in each refinement as well as the "box" used in applying the boundary constraint.

The continuous electron density profiles for the $N=3$ multilayer shows (i) well-defined methyl troughs at $z=0$, 54, and 109 Å; (ii) relatively flat hydrocarbon chain regions for $-24<z<-5$ Å, $2<z<16$ Å, $30<z<37$ Å, $57<z<68$ Å, $85<z<104$ Å; (iii) carboxyl peaks at

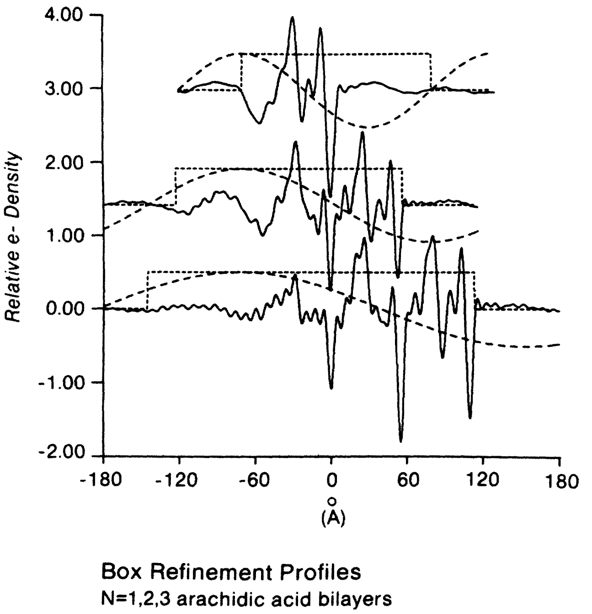

Box Refinement Profiles
N=1,2,3 arachidic acid bilayers

FIG. 7. Box-refinement trial functions (– – – – –), box boundary constraint functions (— — —), and derived multilayer electron density profiles (——) for $N=1,2,3$ *(top to bottom)* bilayer multilayers are shown. These multilayers provide a homologous series for the box-refinement procedure. Note that each profile exhibits features common to each multilayer electron density profile, as well as exhibiting features common to each monolayer within the multilayer electron density profile.

$z=-30$, 23, and 78 Å; and a (iv) disordered, poorly defined methyl trough at $z=70$ Å. The profile for $N=2$ shows (i) well-defined methyl at $z=0$ and 53 Å; (ii) relatively flat hydrocarbon chains regions for $-24<z<-4$ Å, $4<z<20$ Å, $28<z<49$ Å; (iii) carboxyl groups at $z=-29$ and 27 Å; and a (iv) disordered methyl trough at $z=53$ Å. Finally, the profile for $N=1$ shows (i) a well-defined methyl trough at $z=0$ Å; (ii) a relatively flat hydrocarbon chain region for $-5<z<-26$ Å; (iii) a carboxyl group at $z=-31$ Å; and (iv) a disordered methyl trough at $z=-57$ Å. In general, a multilayer profile consisting of N arachidic acid bilayers exhibit N equally spaced well-defined methyl troughs, N equally spaced well-defined carboxyl peaks, and one ill-defined and broad methyl trough at one end. The broadening of this trough causes the hydrocarbon chain region adjacent to the trough to become nonflat. The mean carboxyl-methyl trough distance is 27 Å.

V. DISCUSSION

A. Box refinement

The dotted lines on Figs. 1 and 2 represent the corrected intensity and Patterson functions, respectively, for the one-, two- and three-bilayer multilayers calculated from the multilayer profiles derived by the box-refinement technique. The calculated corrected intensity functions and the calculated multilayer Patterson functions all agree extremely well with the original experimental functions. The calculated intensity function reproduces the shape, the relative intensity, and the position of the diffraction maxima; the fine features of the multilayer Patterson function are also reproduced. The continuous multilayer electron density profiles all show an anomoly at $z=-9$, 47, 104 Å for the $N=1,2,3$ multilayer sample, respectively. This anomoly has the same characteristics in each of the derived profiles; it is a positive spike following the first well-defined methyl trough at one end of the multilayer profile. Each multilayer electron density profile must conform to a reasonable physical-chemical interpretation. All the electron density profiles meet this criteria aside from the above-mentioned anomoly.

To study the anomoly, step-function model electron density profiles equivalent to the continuous multilayer profiles were constructed (Fig. 8). The anomoly is shown as a dashed line in each model. Each step represents ~3 Å in z. The anomaly was attenuated to between 12% and 25% of its original magnitude in the model profiles, from which model intensity functions and model multilayer Patterson functions were calculated and compared to the original corrected intensity functions $I_0(q_z)$ and multilayer Patterson functions $P_{\mathrm{ml}}(z)$.

Figure 9 shows the intensity functions calculated from the continuous multilayer electron density profile, the step-function model profiles, and the original Lorentz-corrected intensity function $I_0(q_z)$ for the $N=2$ multilayer. Note, the excellent agreement between the intensity function derived from the continuous multilayer electron density profile and the experimental intensity function. The step-function models also give good agreement with the experimental intensity function, with some qualifications. By constructing step-function model profiles of

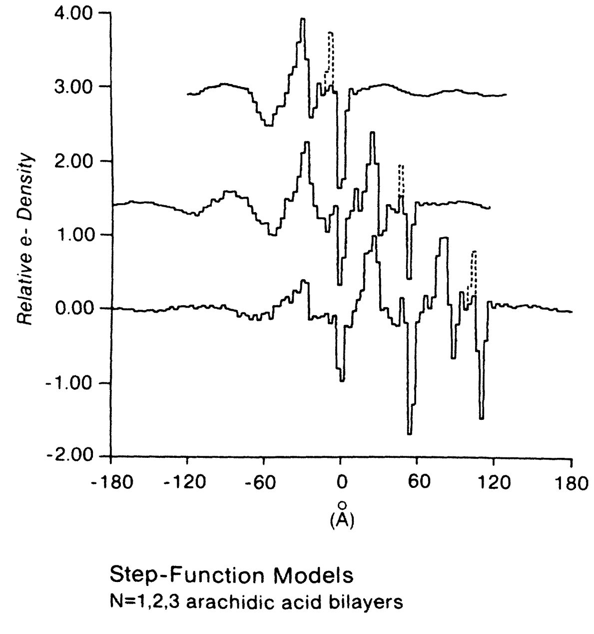

Step-Function Models
N=1,2,3 arachidic acid bilayers

FIG. 8. Step-function models derived from the continuous multilayer electron density profiles shown in Fig. 7. The anomoly (see text) is shown by the dotted line.

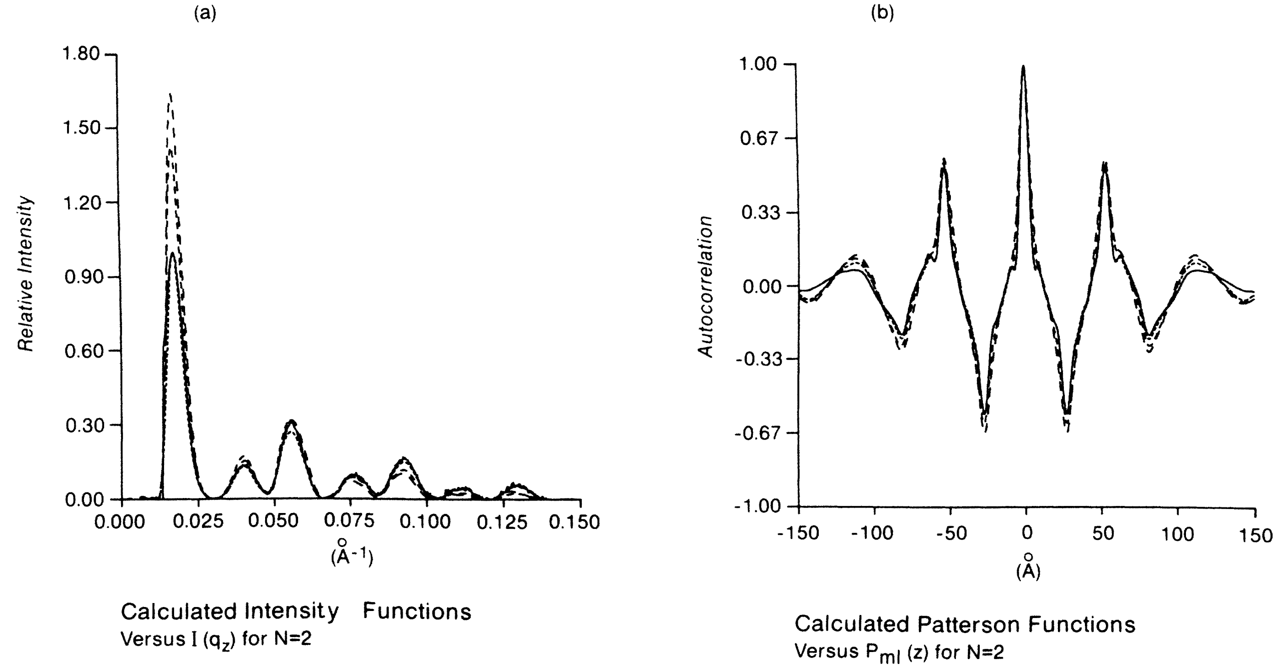

FIG. 9. (a) Calculated Lorentz-q_z corrected intensity functions for the two-bilayer multilayer vs the corrected intensity function, $I_0(q_z)$. The solid line represents the corrected intensity function $I_0(q_z)$; the dotted line (— — —) represents the calculated intensity function from the continuous multilayer electron density profile (Fig. 7) derived by box refinement; the dashed lines represent calculated intensity functions from the step-function models (Fig. 8) without attenuation (— — —) and with attenuation of the anomoly (— —). (b) Calculated multilayer profile Patterson functions for the two-bilayer multilayer vs the multilayer Patterson function derived by Fourier transforming the Lorentz-q_z corrected intensity function. The solid line represents the multilayer Patterson function derived from the corrected experimental intensity function; the dotted line (— — —) represents the multilayer Patterson function calculated from the continuous multilayer electron density profile (Fig. 7) derived by the box-refinement procedure; the dashed lines represent multilayer Patterson functions calculated from the step-function models (Fig. 8) without attenuation of the anomoly (———) and with attenuation of the anomoly (———).

finite spatial resolution, the magnitude of the diffraction maxima for $q_z > 0.075$ Å^{-1} were perturbed; their shape and position remained the same. Differences between the derived model intensity function and the corrected intensity function $I_0(q_z)$ for $N=2$ occur mainly at $q_z \sim 0.02$ Å^{-1} and reflect a different in the magnitude of the first diffraction maximum. Other features of the corrected intensity function including the diffraction maxima shapes, positions, and magnitudes are preserved. As previously mentioned, unavoidable errors in determining the magnitude of the first-order diffraction maxima occur due to the background scattering correction applied to the uncorrected intensity function. Error in the relative magnitude of the first diffraction maxima contributes to errors in the multilayer electron density profiles derived by box refinement. Box refinement cannot compensate for errors in the corrected intensity function, rather it will just refine to them. The origin (with respect to the intensity function) of a particular feature in the continuous multilayer electron density profile can be investigated by perturbing the feature and calculating corresponding intensity functions.

The multilayer Patterson function calculated from the multilayer electron density profile derived by box refinement [Fig. 9(b)] and the multilayer Patterson function $P_{\rm ml}(z)$ calculated from the corrected intensity function $I_0(q_z)$ agree extremely well, as do the step-function model derived multilayer Patterson functions. The step-function model-derived Patterson functions deviate from $P_{\rm ml}(z)$ for $z > 1.5d$ (where d is the "average" periodicity of the multilayer profile). The vectors contributing to the Patterson function for $|z| > 1.5d$ represent correlations between the first and the last monolayer; these correlations correspond primarily to momentum-transfer vectors $q_z < 0.013$ Å^{-1}. This region of momentum-transfer space corresponds to the first diffraction maxima; the magnitude of which is most prone to error in our analysis. The small ringing of the multilayer Patterson function at $|z| > 2d$ is also partially a result of this error and the truncation of the data for $q_z < 0.01$ Å^{-1}. Since the step-function models are of limited spatial resolution the feature at $z = \pm 62$ Å in $P_{\rm ml}(z)$ has become a shoulder on the multilayer Patterson function derived from the step-function models.

Hence, we have shown that errors in $I_0(q_z)$ for $q_z < 0.02$ Å^{-1} are essentially responsible for the anomolies in the box-refinement derived multilayer electron density profiles. However, these errors do not deter the box-refinment technique from determining correctly the general features of the multilayer electron density profiles.

B. Model calculations

It is possible to investigate the derived multilayer electron density profiles further by constructing physical-chemically reasonable, yet mathematically simple multilayer electron density profiles (using only analytical functions) and calculating the meridional intensity and multilayer Patterson functions from these models. While the intensity functions derived from the step-function model profiles described above yield excellent agreement with the experimental intensities, not all their features represent true physical-chemical features in the multilayer electron density profiles. Three types of errors can be seen in these models. The first is a high-frequency oscillation in the electron density profile as a result of only using a finite number of diffraction maxima in the calculations. For example, the step-function model for $N=2$ shows about a 20% oscillation in the magnitude of the electron density profile in the hydrocarbon chain region. This is not physically interpretable, and is probably due to this type of error. The second is a very low-frequency error resulting from errors in truncating $I_0(q_z)$ for $q_z<0.02$ Å^{-1}. The third results from not deconvoluting the beam width function, $W(q_z)$, from the intensity function. This error causes the electron density profile to be modulated by a Gaussian-like function whose full width at half maximum is proportional to the inverse of the FWHM of $W(q_z)$. In a model, it is reasonable to replace the high-frequency oscillations with a constant electron density value and then recalculate the intensity and compare it to the experimental intensity. Other features can also be replaced; the methyl troughs can be fitted with Gaussian functions for instance.

The continuous electron density profiles derived by the box-refinement method yield intensity functions which match the experimental intensity very well [Figs. 1 and 9(a)]. These calculated intensities are zero for $q_z<0.01$ Å^{-1} and $q_z>0.014$ Å^{-1}. While we did not collect data in these regions of momentum-transfer space, the intensity function is not truly zero in those regions.

Before constructing a physical-chemical model for the multilayer profile based on the step-function model electron density profile derived from the box refinement, it is necessary to investigate some of the features of the corrected intensity function, $I_0(q_z)$. We choose to investigate the $N=2$ data for modeling since it was the most accurate with respect to the previously mentioned errors. The first diffraction maxima was reasonably resolved from the specular scattering and the beam-shape function was considerably more narrow than the diffraction maxima. Consider the corrected intensity function for $N=2$ in Fig. 9(a) (solid line). The corrected intensity function has nonzero minima at $q_z=0.048$ Å^{-1} and $q_z=0.085$ Å^{-1}, between diffraction maxima two and three, and maxima four and five, respectively. These nonzero minima can arise from asymmetry in the multilayer electron density profile. The centrosymmetric multilayer profile model discussed earlier (dotted line, Fig. 5) did not reproduce the intensity function very well (dotted line, Fig. 6). In addition, maxima two and three, and four and five are shifted closer together, and are not spaced exactly $1/d$ apart. The shifting of the diffraction maxima occur because the reciprocal lattice function, $|L_n(q_z)|^2$ is not a series of Dirac δ functions, but instead is a sum of sinc^2 functions [Eq. (2)]. Depending on the gradient of the unit-cell structure factor at a particular q_z, diffraction maxima may be shifted when sampled by the reciprocal lattice function $[L_n(q_z)]^2$. Maxima four and six have shoulders at $q_z=0.071$ and 0.107 Å^{-1}, respectively. The shoulder may very well arise from convoluting the beamwidth function with the modulus squared of the multilayer profile structure factor. This beamwidth convolution effectively "smears" the auxiliary maxima into the principal maxima of $|F_{\mathrm{ml}}(q_z)|^2$.

The solid line in Fig. 5 shows an electron density profile model which has some of the features of the centrosymmetric two-bilayer model (dotted line, Fig. 5), but is simpler and asymmetric. The relative magnitudes of the carboxyl peaks ($z=\pm27.5$ Å) compared to the methyl troughs at $z=0$ and $z=56$ Å have been maintained. The hydrocarbon chain regions between the peaks and troughs are now flat. The methyl trough at $z=-56$ Å was broadened and shifted one angstrom toward the center of the multilayer profile. The hydrocarbon chain region for $-42<z<32$ Å also has an average electron density lower than the other hydrocarbon chain regions by about 7.5%. (This is required on physical grounds, namely, an increased area/chain in the plane of the bilayer of the hydrocarbon chain region is required if the methyl trough at $z=-56$ Å is to become broad, shallow, and shifted toward the neighboring carboxyl peak.) The calculated intensity, $I(q_z)$, and its antisymmetric component, $I_A(q_z)$ are shown in Fig. 10. [The square of the cosine transform of the multilayer electron density profile is solely due to

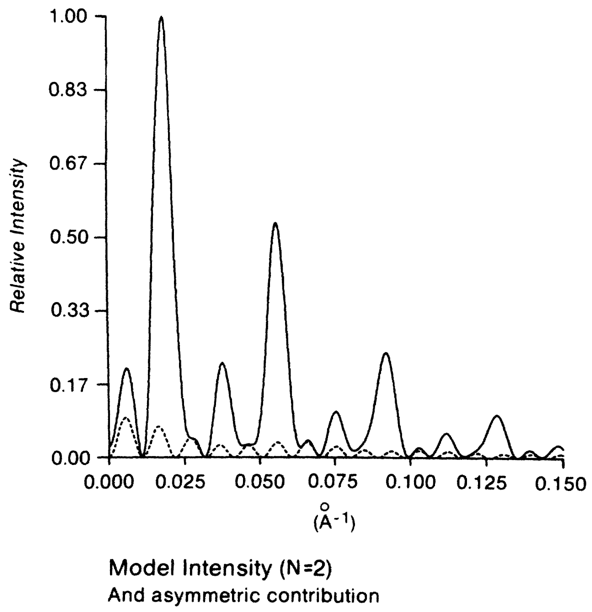

FIG. 10. Calculated intensity function $I(q_z)$ (solid line) for the two- bilayer multilayer and its antisymmetric contribution $I_A(q_z)$ (dotted line). These functions were calculated from the two-bilayer asymmetric model (Fig. 5, solid line) and were not convoluted with the incident beam-shape function.

the symmetric part of the electron density profile and is called the symmetric intensity function, $I_z(q_z)$, while the square of the sine transform of the multilayer electron density profile is solely due to the antisymmetric part of the electron density profile and is called the antisymmetric intensity function $I_A(q_z)$. the intensity function, $I(q_z)$ is just the sum of these symmetric and antisymmetric functions.] Note the nonzero minima at $q_z = 0.046$ Å^{-1} is entirely due to the antisymmetric component of the intensity function, while $I_A(q_z)$ contributes about 50% to the nonzero minima at $q_z = 0.082$ Å^{-1}. Also note the auxiliary maxima at $q_z = 0.061$ and 0.102 Å^{-1} as well as nonzero calculated intensity at $z < 0.01$ and $z > 0.130$ Å^{-1}. The relative intensities and shapes of the diffraction maxima seem to be in reasonable agreement with the corrected intensity function $I_0(q_z)$ [Figs 1 and 9(a)] except for the relative magnitude of the first maxima. As previously mentioned, errors in the magnitude of the first diffraction maxima occur due to errors in background scattering correction. The odd maxima decay with increasing q_z slower than do the even maxima in both the calculated and corrected intensities, with the fourth maximum being about the same magnitude as the second. The seventh maximum is slightly more intense than the sixth; the second is about 50% the magnitude of the third; and the fourth maximum is about 50% of the fifth. The sixth and seventh maxima are about the same magnitude. The nonzero minima have also been reproduced.

The solid line in Fig. 6 shows the calculated intensity function convoluted with the experimental beam-shape function. Note that the auxiliary maxima have flattened and caused the broadening of adjacent maxima. It is especially apparent at $q_z = 0.033$, 0.076, and 0.112 Å^{-1}. Convoluting the calculated intensity function with the experimental beam-shape function makes it nonzero everywhere. However, the calculated intensity function's minima at $q_z = 0.055$ and 0.092 Å^{-1} are above this new baseline, and reproduce the corrected intensity function $[I_0(q_z)]$ fairly accurately [Figs 1 and 9(a)].

The results for the box-refinement method for $N = 1$, 2, and 3 multilayers and the model calculations for $N = 2$ indicate that only one monolayer at one edge of the multilayer is disordered. For the $N = 1$, 2, and 3 multilayers, this one disordered monolayer has a broad shallow methyl trough and a nonflat hydrocarbon chain region characteristic of disordered chains whose average end-end chain length is less than that for *all trans* chains. This series of experiments cannot conclusively determine whether the first monolayer which interfaces the glass OTS surface, or the last monolayer which interfaces air, is the disordered monolayer; however, recently completed experiments on quasiperiodic multilayers containing two types of molecular monolayers of two incommensurate chain lengths[13] demonstrate that it is indeed the air interfaced monolayer which has been disordered. This result is not surprising when one considers that the OTS hydrocarbon chain is very similar (on a macromolecular level) to that of arachidic acid. Deposition of the first arachidic acid monolayer onto the glass OTS surface should not be very different (with respect to intermolecular forces between monolayers) than depositing the third monolayer onto the second, or the fifth onto the fourth, etc. The last monolayer is not constrained by the terminal methyl groups of a juxtaposed monolayer. The chain terminal methyl groups of the last monolayer interface with air; consequently these chains appear to have more degrees of freedom than the chain terminal methyl groups of the internal monolayers in the multilayer.

The narrow features in the rocking curves shown in Fig. 1(a) are most likely due to the well-oriented domains of the multilayers and the broad features are probably a result of misoriented components. The relative contribution of oriented versus misoriented domains in the multilayers remain fairly constant for $N = 1$ to 5.

VI. CONCLUSION

The $N = 1,2,3$ multilayer specimens provide a homologous series for the box-refinement technique. While there is no guarantee that the box refinement converged to the correct solution in each case, the fact that three vastly different corrected intensity functions $I_0(q_z)$ refined to quantitatively analogous multilayer electron density profiles is strong evidence that the refinement did indeed converge to the correct solution in each case. Furthermore, a mathematically simple and physical-chemically reasonable model has been constructed for the $N = 2$ case which further clarifies the box-refinement result. Additional evidence supporting the validity of the box-refinement solutions comes from the fact that the results are consistent with the average bilayer electron density profiles derived from the deconvolution of the multilayer Patterson function $P_{\text{ml}}(z)$. The Patterson-function deconvolution technique employing the Fourier synthesis gives bilayer profile structures which represent the average structure of the bilayer ensemble. As the number of bilayers decreases, the average bilayer electron density profile becomes more sensitive to perturbations in any given bilayer. It is therefore consistent that the average bilayer electron density profile for $N = 2$, 3, and 5 represents a more well-ordered system as N increases, if the number of perturbed bilayers (or monolayers) in the multilayer remains constant.

The Patterson deconvolution technique can lead to an erroneous conclusion concerning the multilayer electron density profiles of the arachidic acid and multilayers; namely, that as the number of bilayers decrease, the multilayer of N repeating average unit-cell bilayers as a whole disorders. The box-refinement procedure demonstrated that only the last monolayer was in fact disordered. This verifies that the assumption used in the Patterson-function deconvolution technique (the existence of a repeated unit cell or bilayer) was incorrect.

We[14] and Pomerantz *et al.*[1] have shown that the auxiliary maxima observed in the meridional diffractional data can be well resolved by improving Δq_z resolution. This requires improved detector spatial resolution and x-ray optics, or requires an increase in specimen to detector distance with focusing x-ray optics. The latter generally necessitates either greater x-ray flux or extended total exposure time to maintain the statistical accuracy of the data. Improving both the statistical accuracy of the data and the Δq_z resolution of the experimental system is essential in the structural study of multilayer thin films by x-ray diffraction techniques since the methods of data analysis employed depend critically on these parameters.

The Langmuir-Blodgett technique is a very powerful tool in creating multilayer systems composed of a finite number of monolayers, each of a defined chemical composition. X-ray diffraction can now be used to probe the structure of such multilayer systems, even to the level of one bilayer or individual monolayer. The box-refinement analysis (provided one uses a homologous series of multilayers) can yield excellent results in determining the multilayer electron density profiles for each of the series in the absence of the stringent requirement that the multilayer be composed of a finite number of repeated symmetric units, e.g., symmetric bilayers, bilayer pairs, etc. It provides the investigator with a tool that can probe the structure of each individual monolayer in the electron density profile of the multilayer. Substrate induced monolayer ordering or disordering can also now be studied by this technique.

ACKNOWLEDGMENTS

This work was supported by the National Institute of Health (NIH) Grant No. GM-33525, the National Science Foundation (NSF) materials Research Laboratories Program Grant No. DMR-82-16718, and the U.S. Air Force Office of Scientific Research (AFOSR) Grant No. 84-0135.

---

[*] Present address: Department of Biochemistry and Biophysics, University of California at San Francisco, 513 Parnassus Avenue, San Francisco, CA 94143-0554.

[1] M. Pomerantz and A. Segmüller, Thin Solid Films **68**, 33 (1980).

[2] W. Lesslauer and J. K. Blasie, Biophys. J. **12**, 175 (1972).

[3] T. J. McIntosh, R. C. Waldbilling, and J. D. Robertson, Biochim. Biophys. Acta **448**, 15 (1976).

[4] R. M. Stroud and D. A. Agard, Biophys. J. **25**, 495 (1979).

[5] L. Makowski, J. Appl. Cryst. **14**, 160 (1981).

[6] K. B. Blodgett, JACS **57**, 1007 (1935).

[7] J. Sagiv, JACS **102**, 92 (1980).

[8] J. R. Milch, IEEE Trans. Nucl. Sci. **26**, 338 (1979).

[9] S. M. Gruner, J. R. Milch, and G. T. Reynolds, Rev. Sci. Instrum. **53**, 1770 (1972).

[10] R. Hoseman and S. N. Bagchi, *Direct Analysis of Diffraction by Matter* (North-Holland, Amsterdam, 1962).

[11] S. Schwartz, J. E. Cain, E. A. Dratz, and J. K. Blasie, Biophys. J. **15**, 1201 (1975).

[12] W. Lesslauer, J. Cain, and J. K. Blasie, Biochim. Biophys. Acta **241**, 547 (1971).

[13] V. Skita, W. Richardson, M. Filipkowski, A. F. Garito, and J. K. Blasie, J. Phys. (Paris) (to be published).

[14] W. Lesslauer and J. K. Blasie, Acta Cryst. A **27**, 456 (1971).